Bending Magnet Synchrotron Radiation Imaging with Large Orbital Collection Angles

M. Labat,[1,*] O. Chubar,[2] J. Breunlin,[3] N. Hubert,[1] and Å. Andersson[3]
[1]*Synchrotron SOLEIL, L'Orme des Merisiers, 91 190 Saint-Aubin, France*
[2]*Brookhaven National Laboratory, Building 741, P.O. Box 5000, Upton, New York 11973-5000, USA*
[3]*MAX IV Laboratory, P.O. Box 118, SE-221 00 Lund, Sweden*

(Received 24 December 2022; revised 16 July 2023; accepted 22 August 2023; published 1 November 2023)

Synchrotron radiation (SR) from bending magnets, wigglers, and undulators is now extensively produced for users at storage ring based light sources, with unique properties in terms of average brightness and stability. We present a profound study of bending magnet SR intensity distribution in the image plane of a focusing optical system. Measurements of this intensity distribution at the MAX-IV low emittance storage ring are compared to theoretical predictions, and found to be in excellent agreement. This work shows upon the possibility of performing high resolution emittance diagnostics with visible or near-visible SR on upcoming low-emittance storage ring based light sources. As a byproduct of our study, we derive a closed analytical expression for the intensity distribution from a zero-emittance beam, in the limiting case of wide orbital collection angles. This expression finally allows us to demonstrate the meeting between classical electrodynamics applied to SR emission and focusing, and the Landau and Lifshitz prediction of radiation intensity distribution nearby a caustic.

DOI: 10.1103/PhysRevLett.131.185001

Synchrotron radiation (SR) is produced by ultrarelativistic electrons moving in an external magnetic field. Predicted by classical electrodynamics, it was first observed in the early 1940s [1] thanks to the advent of accelerators for high-energy physics. Initially considered as a side effect causing energy loss and eventually limiting the maximum energy attainable on those accelerators, SR was initially only described in terms of its total power relying on Larmor's formula [2,3]. The first derivations of the SR angular and spectral distribution were given in the late 1940s [4,5]. In the frame of classical electrodynamics, the authors used the retarded potential approach [6,7] to describe the SR electric field for an observer far from the source current location, i.e., the electron beam. This approach has since remained as a reference [8].

In spite of its undesirable beginnings, SR was rapidly revealed to be of high interest. Modern storage ring based light sources are now accelerator facilities optimized for the delivery of high brightness SR to users. The radiation is generated in the magnetic field of undulators, wigglers, and bending magnets (BMs) [9] installed all around the storage ring. The fields of application for SR are extremely vast and keep extending, from material science [10] to archeology [11], biology [12] and chemistry [13], and to medicine [14].

In the early 1980s, high intensity and high resolution applications of SR raised a significant interest in modeling the SR distribution in the image plane of a focusing element. But due to SR intrinsic features, this modeling was revealed as being rather complex. SR is emitted indeed within a small opening angle, leading to pronounced diffraction phenomena and all along curved trajectories, leading to pronounced depth-of-field effects. In the case of a bending magnet magnetic field, SR is emitted along an arc of a circle. First descriptions of BM SR intensity distribution in the image plane of a focusing element clearly addressed the key role played by diffraction and depth of field, however, treating each of these effects separately [15–18]. In a more general, retarded potentials based approach, diffraction integrals describing focused BM SR were derived and used to compute electric field and intensity distributions of the radiation in the image plane of an electron beam profiler [19]. Preserving the radiation phase information as the electron moves along its trajectory, this method naturally included all features inherent to BM SR and paved the way to accurate BM SR imaging simulations [20]. The role of the horizontal collection angle on the final BM SR image distribution was then pointed out in [21,22]. Even though relying on different SR modelings (Gaussian wave optics in [21] and general electrodynamics in [22]), authors simultaneously revealed that the intensity distribution in the image plane is strongly distorted along the horizontal axis by one-sided fringes when the horizontal collection angle becomes larger than the SR natural opening angle. This extended source effect is related to one specific phase term in the diffraction integral expression of the SR electric field [21–23]. Since 1996, experimental measurements of distorted BM SR images have been continuously reported on MAX-II, MAX-III, and SLS storage rings [20,24–26], and the distortion features have even been proposed to be used for horizontal beam size diagnostic purposes [27,28].

In this Letter, we present a profound study of bending magnet SR intensity distribution in the image plane of a lens. More specifically, we explore the behavior of the BM SR intensity distribution between extreme horizontal collection angle limits. Both the Synchrotron Radiation Workshop (SRW) numerical code [29], with built-in capabilities to simulate finite beam emittance properties, and analytical expressions for a zero-emittance beam, are confronted with success to measurements on the MAX-IV low emittance storage ring. The excellent agreement we obtain between models and experiment supports the validity of classical electrodynamics for modeling SR emission and focusing on storage rings. Moreover, the blurring of the fringe pattern observed at large orbital plane angles is proven to be tightly correlated to the electron beam emittance. This strongly indicates that emittance diagnostics with visible or near-visible SR will remain an accurate alternative at fourth generation storage ring based light sources with ultralow emittances when usual x-ray based measurements reach their resolution limits. While exploring the beam diagnostics benefits of using wide horizontal collection angles, we finally derive a new closed analytical expression for wide enough angles, and demonstrate the meeting of classical electrodynamics applied to SR emission and focusing, with Landau and Lifshitz prediction of radiation intensity distribution nearby a caustic. We find this to be a surprising and valuable finding.

The basic layout for the observation of BM SR in the image plane of a focusing element is depicted in Fig. 1. Electrons in the constant magnetic field of a BM follow a circular trajectory with a radius of curvature ρ. For the sake of simplicity, the focusing element is assumed to be a perfect lens. The collection angles are referred as $\Delta\theta_x$ in the horizontal and $\Delta\theta_y$ in the vertical plane. The SR emitted at a wavelength λ has a natural opening angle of $\Delta\theta_{\mathrm{SR}} = (\lambda/\rho)^{1/3}$ if $\lambda \gg \lambda_c$, and $\lambda_c = 4\pi\rho/(3\gamma^3)$ is the critical SR wavelength.

For ease of reading, we only summarize here our analytical derivation of the BM SR intensity distribution in the image plane of a lens for a zero-emittance beam (see complete derivation in Supplemental Material, Sec. A [30]). In the frame of classical electrodynamics using the retarded potential approach [6,7], the exact expression in the frequency domain of the SR electric field $E_0(\omega)$ at frequency $\omega = 2\pi c/\lambda$ can be derived, where c is the speed of light. After geometric expansion of the electric field phase in terms of (small) horizontal and vertical angles in the far field, a closer expression of $E_0(\omega)$ is obtained, where σ and π polarized components can be distinguished. In the following, we only retain the σ polarization component but equivalent results can be obtained for the π component. Using Fourier optics for backpropagation to the source point, equivalent to forward propagation to the image plane, we end up with a first expression of the SR electric field in the image plane of a lens $E_\sigma(x, y, \lambda)$, where $(x,\ y)$ are, respectively, the horizontal and vertical coordinates in the image plane. After reduction using the derivative of the Airy function Ai′ [31], $E_\sigma(x, y, \lambda)$ in Gaussian centimetre–gram–second units becomes

$$
\begin{aligned}
E_\sigma(x,y,\lambda) = {} & -\frac{4i\pi^{4/3}e\rho^{1/3}}{c\lambda^{4/3}} \\
& \times \int_{\Delta\theta_y} \mathrm{Ai}'\left[\left(\frac{\pi\rho}{\lambda}\right)^{2/3}(\gamma^{-2}+\theta_y^2)\right]\exp\left(\frac{2\pi i y}{\lambda}\theta_y\right) \\
& \times \int_{\Delta\theta_x} \exp\left[\frac{i\pi\rho\theta_x}{\lambda}(\gamma^{-2}+\theta_x^2/3+\theta_y^2)+\frac{2\pi i x}{\lambda}\theta_x\right] \\
& \times d\theta_x d\theta_y, \qquad (1)
\end{aligned}
$$

assuming a $M = 1$ magnification by the lens. Note that Eq. (1) meets the result of the somewhat different derivation found in [21], as well as the phase term prediction of [22]. The intensity in photons per second per unit relative bandwidth per unit surface area $I_\sigma(x, y, \lambda)$ is simply related to $E_\sigma(x, y, \lambda)$ according to

$$
I_\sigma(x,y,\lambda) = \frac{c^2\alpha I}{4\pi^2 e^3}|E_\sigma(x,y,\lambda)|^2, \qquad (2)
$$

with α the fine-structure constant and I the electron current.

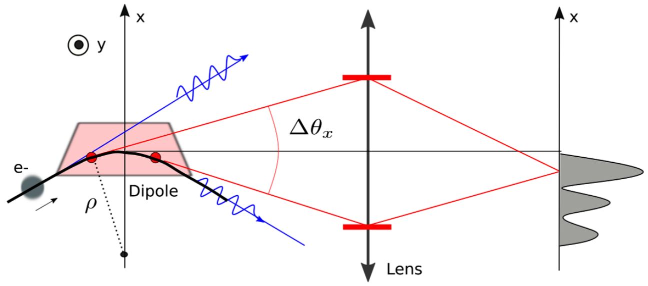

FIG. 1. Experimental setup for the observation of BM SR in the image plane of a focusing lens. Blue lines: synchrotron radiation emitted inside the dipole. Red lines: horizontal SR collection angle $\Delta\theta_x$. Gray plot: sketched BM SR intensity profile along x in the image plane.

Our measurements were performed on the MAX-IV 3 GeV electron storage ring [27,28]. Being the first fourth generation storage ring based on a multibend achromat magnetic lattice, MAX-IV offers a low emittance of 328 pm rad in the horizontal plane. Thanks to this low emittance, the fringe pattern described by Eqs. (1) and (2) can be, for the first time ever, observed experimentally without being blurred out completely by the beam emittance. The B302 beamline of MAX-IV was designed to enable imaging the BM SR up to large collection angles ($\Delta\theta_x$ up to 15 mrad, $\Delta\theta_y$ up to 7 mrad). The imaging is achieved with a high surface accuracy fused silica planoconvex lens, while bandpass filters are used to monochromatize the photon beam and a Glan-Taylor polarizer is used to retain the σ

component. The final two-dimensional light sensitive detector, located in the image plane, is a CMOS based commercial camera.

It is clear from Eqs. (1) and (2) that the BM SR intensity distribution in the image plane strongly depends on the collection angles $\Delta\theta_x$ and $\Delta\theta_y$. As a first representation of the focused BM SR peculiarities, we consider a limited, but rather large, $\Delta\theta_y$ collection angle (7 mrad as in the experiment) and vary $\Delta\theta_x$ from 1 to 20 mrad. The results are presented in Fig. 2, with the data from Eqs. (1) and (2) shown in row (a) and the experimental results shown in row (c), while varying $\Delta\theta_x$ along the columns (i)–(iii). For small $\Delta\theta_x$ (i), typically $\Delta\theta_x < \Delta\theta_{\mathrm{SR}}$, $I_\sigma(x, y, \lambda)$ is quasisymmetric around $x = 0$ and $y = 0$ axes (white lines across the panels). The horizontal intensity distribution follows a sinc^2 dependence, as expected for Fraunhofer-like diffraction by the small $\Delta\theta_x$ aperture. When $\Delta\theta_x$ increases (ii), typically $\Delta\theta_x > \Delta\theta_{\mathrm{SR}}$, the main intensity peak tends to shift toward negative x values while vertically curved fringes of descending intensity develop along $x < 0$. These fringes are enhanced at further increase of $\Delta\theta_x$ (iii) because the second integrand phase term of Eq. (1) exhibits a component in θ_x^3 which becomes dominant for large $\Delta\theta_x$ collection angles. One can also intuitively understand these fringes as resulting from the interference between waves generated along upstream and downstream parts, with respect to the tangential source point, of the electron trajectory [21,32] (see Fig. 1).

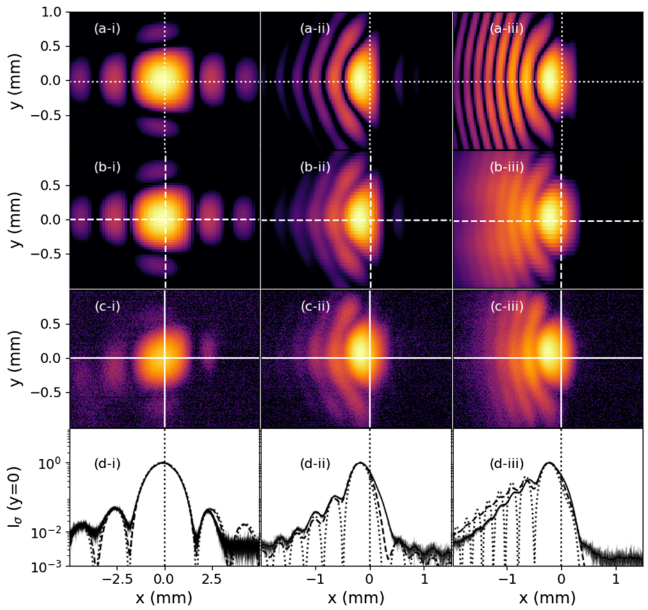

FIG. 2. (a)–(c) Intensity distributions $I_\sigma(x, y, \lambda)$ in the image plane for three different horizontal collection angles $\Delta\theta_x$ from (a) Eq. (1), (b) SRW simulations, and (c) experimental measurements using $\Delta\theta_y = 7$ mrad. Column (i) $\Delta\theta_x = 1.57$ mrad, column (ii) $\Delta\theta_x = 8.85$ mrad, and column (iii) $\Delta\theta_x = 15.57$ mrad. Images are in logarithmic scale to enhance the agreement. (d) On-axis ($y = 0$) horizontal profiles along the x white lines of (a)–(c) using the same line style (for experimental measurements, single shots are in gray thin lines while their average is in dark line). Related parameters are $\epsilon_x = 328$ pm rad, $\epsilon_y = 8$ pm rad, $\gamma = 5870$, energy spread $\sigma_e = 0.077\%$, $\beta_x = 1.19$ m, $\beta_y = 8.63$ m (for the ideal machine), $\eta_x = 25$ mm, $\eta_y < 0.2$ mm (measured), $\rho = 18.96$ m, $M = 3.0$, and $\lambda = 930$ nm. For experimental records: CMOS camera and bandpass filter of 10 nm FWHM bandwidth centered at 930 nm.

Whatever $\Delta\theta_x$, the measured patterns remarkably follow the predictions of Eqs. (1) and (2) with the exception of the contrast of the fringes, significantly blurred in the experimental case. Equations (1) and (2) were indeed derived for a *filament* (zero transverse emittance) electron beam. To take into account the experimental nonzero transverse emittance, the intensity in Eq. (2) has to be convolved with the particle density distribution of the electron beam, projected onto the image plane of the optical system. Such processing can be done using SRW numerical code as shown in row (b) of Fig. 2. We first verified that using a zero emittance beam, SRW provides exactly the same intensity distribution in the image plane as our model (not shown). The emittance was then increased under SRW, leading to a progressive blurring of the fringe pattern as shown in row (b) of Fig. 2. Best matching with experiment using $\Delta\theta_x = 8.85$ mrad, was reached for $\epsilon_x = 336$ pm rad, i.e., very close to the emittance of the ideal machine $\epsilon_x = 328$ pm rad. Such an agreement between theory and experimental measurement confirms that fringe pattern blurring can be used for the accurate measurement of the true horizontal beam size, as assumed in [24,27,28].

With a willingness to investigate further the BM SR peculiarities in the image plane, we define the following key observables: (i) T_M and T_m the pseudo-periods of the fringes, i.e., the distances between, respectively, the first two maximum and minimum intensity locations at $y = 0$, (ii) R_1 and R_2 the intensity ratios between the first maximum and, respectively, the second and third maxima of intensity, (iii) δx the x shift amplitude of the maximum intensity location. In Fig. 3, the dependency of the BM SR intensity distribution on λ is illustrated for a given set of $\Delta\theta_{x,y}$. In row (a) are shown the 2D intensity distributions recorded experimentally (scaled to unity magnification) for an increasing λ, while in (b) is summarized the comparison between the modeled and experimentally measured $T_{M,m}$ pseudo-periods. The measurements notably follow the Eq. (1) prediction, revealing an increase of the pseudo-periods with λ.

In Fig. 4, the focused BM SR features are *explored* between the $\Delta\theta_{x,y} \to 0$ and $+\infty$ limits. When $\Delta\theta_x$ increases, the pseudo-periods $T_{M,m}$ [Fig. 4(a)] and the intensity ratios $R_{1,2}$ [Fig. 4(b)] decay, while the x shift amplitude δx [Fig. 4(c)] smoothly increases before ending with descending oscillations around an asymptotic value. Those oscillations result from the θ_x^3 term in Eq. (1) and were confirmed with SRW simulations (see Supplemental

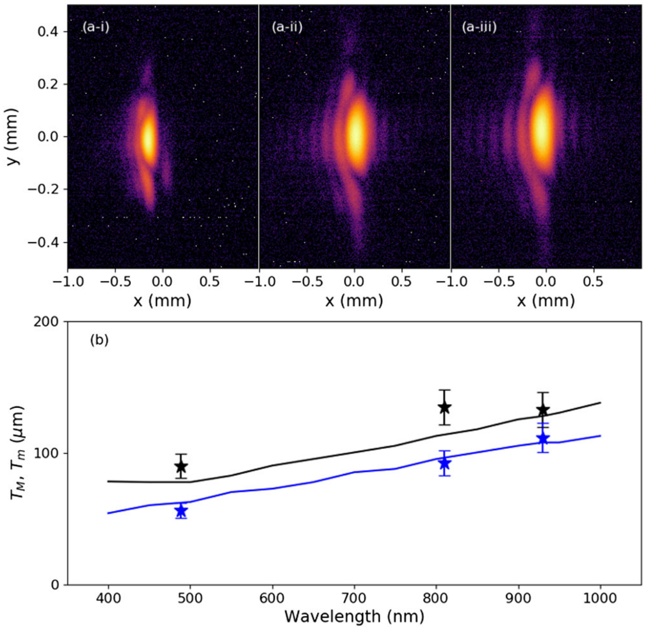

FIG. 3. (a) Measured intensity distributions $I_\sigma(x, y, \lambda)$ (scaled to unity magnification) for (i) $\lambda = 488$ nm, (ii) $\lambda = 810$ nm, (iii) $\lambda = 930$ nm using $\Delta\theta_x = 6.6$ mrad and $\Delta\theta_y = 7$ mrad. (b) Pseudo-periods T_M (in black) and T_m (in blue) extracted along $y = 0$ axis using $\Delta\theta_x = 11$ mrad and $\Delta\theta_y = 7$ mrad from (asterisk) experimental measurements and (—) Eq. (1). Experimental setup: bandpass filters of 10 nm–FWHM bandwidth centered at 488, 810, and 930 nm. Other parameters as in Fig. 2.

Material, Sec. B [30]). Once again, experimental measurements (asterix) and model predictions (continuous lines) are found to be in remarkable agreement. It also clearly appears that all observables tend to stabilize above typically $\Delta\theta_x > 5 \times \Delta\theta_{\mathrm{SR}}$, i.e., converge when $\Delta\theta_x \to +\infty$. In this limit, Eq. (2) can be indeed reduced to

$$
\begin{aligned}
I_\sigma(x, y, \lambda) &\propto |E_\sigma(x, y, \lambda)|^2 \\
&\propto \left| \int_{\Delta\theta_y} \mathrm{Ai}'\left[\left(\frac{\pi\rho}{\lambda}\right)^{2/3}(\gamma^{-2} + \theta_y^2)\right] \exp\left(\frac{2\pi i y}{\lambda}\theta_y\right) \right. \\
&\quad \left. \times \mathrm{Ai}\left[2^{1/3}\frac{(\gamma^{-2} + \theta_y^2)\rho/2 + x}{\rho^{1/3}(\lambda/(2\pi))^{2/3}}\right] d\theta_y \right|^2. \qquad (3)
\end{aligned}
$$

When $\Delta\theta_x \to +\infty$, the BM SR intensity $I_\sigma(x, y, \lambda)$ tends toward the Airy function along x with no $\Delta\theta_x$ dependence. The prediction of this simplified expression is featured as filled circles in Fig. 4, and indeed matches the convergence points of all three observables.

When now $\Delta\theta_y$ is scanned from 0 to $+\infty$, surprisingly, neither the pseudo-periods $T_{M,m}$ nor the intensity ratios $R_{1,2}$ significantly depend in $\Delta\theta_y$, so that the trends of Figs. 4(a) and 4(b) remain nearly the same whatever $\Delta\theta_y$ (not displayed for the sake of clarity). In contrast, the shift amplitude δx is very sensitive to $\Delta\theta_y$ [see Fig. 4(c)].

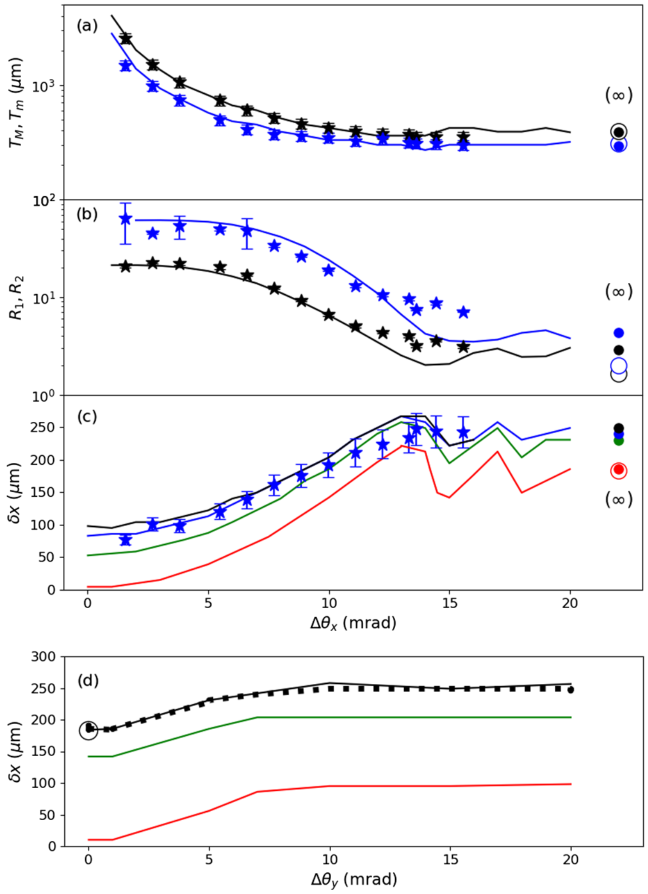

FIG. 4. (a)–(c) Focused BM SR features versus $\Delta\theta_x$ with in (a) pseudo-periods T_M (in black) and T_m (in blue), (b) intensity ratios R_1 (in black) and R_2 (in blue), (c) δx. (d) δx versus $\Delta\theta_y$. Observables extracted from (asterix) experimental measurements, (—) Eq. (1), (filled circle) and (thick dashed line) Eq. (3), and (empty circle) Eq. (4). (a),(b) $\Delta\theta_y = 7$ mrad. (c) $\Delta\theta_y$ is 1 mrad (red line), 5 mrad (green line), 7 mrad (blue line), and 15 mrad (black line). (d) $\Delta\theta_x$ is 1 mrad (red line), 10 mrad (green line), and 20 mrad (black line). Other parameters as in Fig. 2.

Plotting δx against $\Delta\theta_y$ for three different $\Delta\theta_x$ [see Fig. 4(d)] reveals that this dependence is monotonic and that above few $\Delta\theta_{\mathrm{SR}}$ ($\approx$10 mrad), the $\Delta\theta_y$ dependence ceases and the asymptotic value is reached. Unfortunately, we did not manage to reduce Eq. (3) to a simpler expression for $\Delta\theta_y \to +\infty$. However, for $\Delta\theta_y \to 0$ around $y = 0$ and observing that the submicron horizontal displacement $x = \rho/2\gamma^2$ can be neglected in our case, Eq. (3) simplifies to

$$
I_{\sigma-LL}(x) \propto \mathrm{Ai}^2\left[2^{1/3}\frac{x}{\rho^{1/3}[\lambda/(2\pi)]^{2/3}}\right]. \qquad (4)
$$

The predictions of Eq. (4) are featured as empty circles in Fig. 4. The asymptotic values of δx for $\Delta\theta_x \to +\infty$ and $\Delta\theta_y \to 0$ [Figs. 4(c) and 4(d)] well match the more practical values for $\Delta\theta_x = 20$ mrad and $\Delta\theta_y = 1$ mrad.

The $T_{M,m}$ observables are also very well described by Eq. (4), already at $\Delta\theta_x = 15$ mrad [Fig. 4(a)], while the observables $R_{1,2}$ slightly deviate [Fig. 4(b)], as unsurprisingly, since here $\Delta\theta_y$ is 7 mrad, far above zero.

Unexpectedly, Eq. (4) exactly corresponds to one of the hundred-years-back predictions from Landau and Lifshitz. Using the framework of scalar diffraction theory, Landau and Lifshitz accurately described the propagation of light rays nearby a caustic, i.e., a curve—or a surface—to which each light ray is tangent, defining an envelope of concentrated light. Their final expression of the radiation intensity distribution at a distance x from a caustic with a radius of curvature ρ exactly corresponds to our Eq. (4). Since BM SR is emitted tangentially to the circular trajectory of electrons, the analogy with a caustic is, afterward, evident.

In summary, we presented an extensive study of the BM SR intensity—quite extreme—distribution features observed in the image plane of a focusing element. This work confirms that we have at hand outstanding new possibilities (as was also indicated in [18–23,27]) for high resolution beam size diagnostics with visible or near-visible SR on fourth generation, low-emittance, storage ring light sources. By deriving a new analytical formula in the extreme case of large collection angles in the orbital plane, we also demonstrated the meeting between classical electrodynamics modeling of focused SR and the Landau and Lifshitz prediction of intensity distribution nearby a caustic, a surprising and valuable finding.

O. C. acknowledges funding from US DOE Office of Science, Program of Basic Energy Sciences, under FWP PS-017 grant, for work on the development of SRW code.

---

[*]marie.labat@synchrotron-soleil.fr

[1] F. R. Elder, A. M. Gurewitsch, R. V. Langmuir, and H. C. Pollock, Radiation from electrons in a synchrotron, Phys. Rev. **71**, 829 (1947).

[2] D. Iwanenko and I. Pomeranchuk, Radiation from electrons in a synchrotron, Akad. Nauk. Dokl. **44**, 315 (1944).

[3] D. Iwanenko and I. Pomeranchuk, On the maximal energy attainable in a betatron, Phys. Rev. **65**, 343 (1944).

[4] D. Ivanenko and A. Sokolov, On the theory of the "luminous" electron, DAN (U.S.S.R.) **59**, 1551 (1948).

[5] J. Schwinger, On the classical radiation of accelerated electrons, Phys. Rev. **75**, 1912 (1949).

[6] A. Liénard, L'éclairage electrique, Champ électrique et Magnétique **16**, 5 (1898).

[7] E. Wiechert, Elektrodynamische Elementargesetze, Arch. Neerl. Sci. Exactes Nat. **5**, 549 (1900).

[8] J. Jackson, *Classical Electrodynamics* (Wiley, New York, 1975).

[9] J. Kirz, D. Attwood, B. Henke, M. Howells, K. Kennedy, and K. Kim, *X-Ray Data Booklet*, 1st ed. (Lawrence Berkeley Laboratory, Berkeley, CA 94720, 1985), Vol. 1, Sec. IV.

[10] G. S. Knapp, M. A. Beno, and H. You, Hard x-ray synchrotron radiation applications in materials science, Annu. Rev. Mater. Sci. **26**, 693 (1996).

[11] U. Bergmann, P. Manning, and R. Wogelius, Chemical mapping of paleontological and archeological artifacts with synchrotron x-rays, Annu. Rev. Anal. Chem. **5**, 361 (2012).

[12] M. Grabowski, D. R. Cooper, D. Brzezinski, J. M. Macnar, I. G. Shabalin, M. Cymborowski, Z. Otwinowski, and W. Minor, Synchrotron radiation as a tool for macromolecular x-ray crystallography: A XXI century perspective, Nucl. Instrum. Methods Phys. Res., Sect. B **489**, 30 (2021).

[13] F. Meirer and B. Weckhuysen, Spatial and temporal exploration of heterogeneous catalysts with synchrotron radiation, Nat. Rev. Mater. **3**, 1 (2018).

[14] Y. Prezado and I. Martínez-Rovira, Medical applications of synchrotron radiation, Radiat. Damage Biomol. Syst. 433 (2012).

[15] A. Hofmann and F. Méot, Optical resolution of beam cross-section measurements by means of synchrotron radiation, Nucl. Instrum. Methods Phys. Res. **203**, 483 (1982).

[16] K.-J. Kim, Brightness, Coherence and propagation characteristics of synchrotron radiation, Nucl. Instrum. Methods Phys. Res., Sect. A **246**, 71 (1986).

[17] J. MacKay, Electron beam profile, position systems and measurements on the Daresbury SRS, Preprint Daresbury Laboratory DL/SCI/P591A (1988).

[18] A. Ogata, On optical resolution of beam size measurements by means of synchrotron radiation, Nucl. Instrum. Methods Phys. Res., Sect. A **301**, 596 (1991).

[19] O. Chubar, Resolution improvement in beam profile measurements with synchrotron light, in *Proceedings of International Conference on Particle Accelerators* (IEEE, Washington DC, 1993), Vol. 3, p. 2510.

[20] Å. Andersson, M. Eriksson, and O. Chubar, Beam profile measurements with visible synchrotron light on MAX-II, *Proceedings of EPAC'96, Fifth European Particle Accelerator Conference* (JACOW, Geneva, Switzerland, 1996), p. 1689.

[21] R. Bosch, Focusing of infrared edge and synchrotron radiation, Nucl. Instrum. Methods Phys. Res., Sect. A **431**, 320 (1999).

[22] O. Chubar, P. Elleaume, and A. Snigirev, Phase analysis and focusing of synchrotron radiation, Nucl. Instrum. Methods Phys. Res., Sect. A **435**, 495 (1999).

[23] N. Smolyakov, Wave-optical properties of synchrotron radiation, Nucl. Instrum. Methods Phys. Res., Sect. A **405**, 235 (1998).

[24] Å. Andersson, Electron beam profile measurements and emittance manipulation at the MAX-laboratory, Ph.D. thesis, Lund University, Sweden, 1997.

[25] Å. Andersson, M. Böge, A. Lüdeke, V. Schlott, and A. Streun, Determination of a small vertical electron beam profile and emittance at the Swiss Light Source, Nucl. Instrum. Methods Phys. Res., Sect. A **591**, 437 (2008).

[26] A. Hansson, E. Wallén, and Å. Andersson, Transverse electron beam imaging system using visible synchrotron

radiation at MAX III, Nucl. Instrum. Methods Phys. Res., Sect. A **671**, 94 (2012).

[27] J. Breunlin, Emittance related topics for fourth generation storage ring light sources, Ph.D. thesis, Lund University, https://lucris.lub.lu.se/ws/portalfiles/portal/11915390/Thesis_Breunlin.pdf (2016).

[28] J. Breunlin and Å. Andersson, Emittance diagnostics at the MAX IV 3 GeV storage ring, in *Proceedings of the 7th International Particle Accelerator Conference* (JACOW, Geneva, Switzerland, 2016), p. WEPOW034.

[29] O. Chubar and P. Elleaume, Accurate and efficient computation of synchrotron radiation in the near field region, in *Proceedings of EPAC'98, Stockholm* (JACOW, Geneva, Switzerland, 1998), p. 88.

[30] See Supplemental Material at http://link.aps.org/supplemental/10.1103/PhysRevLett.131.185001 for detailed analytical derivation of BM SR intensity distribution in the image plane of a focusing lens.

[31] Bessel-type functions, https://functions.wolfram.com/Bessel-TypeFunctions/AiryAiPrime/07/01/01/.

[32] X. Artru, Impact parameter profile of synchrotron radiation, in *Advanced Radiation Sources and Applications*, edited by H. Wiedemann (Springer Netherlands, Dordrecht, 2006), pp. 387–398.